Supplementary Material of :

Bending, Nanoindentation and Plasticity Noise in FCC single and poly crystals.

R. Bolin[b], H. Yavas[a,d], H. Song[a,b], K. J. Hemker[a], S. Papanikolaou[a,b,c*]

[a] Department of Mechanical Engineering, Johns Hopkins University, Baltimore, MD 21216

[b] Department of Mechanical and Aerospace Engineering, West Virginia University, Morgantown, WV 26506

[c] Department of Physics, West Virginia University, Morgantown, WV 26506

[d] Department of Control Engineering, Faculty of Electrical Engineering, Czech Technical University in Prague, Technika 2, Prague 6, Czech Republic

In this supplementary material, we describe further details on our experimental methods and results. Also, we present results from finite element simulations and discrete dislocation dynamics simulations that corroborate the experimental results of the main text.

S1. Bending device and FEM simulations

The actual image of the 4-pt bending stage in shown in Figure 1(a) and Figure 1(c). This apparatus is composed of a single block steel base and a movable stress plate where in-plane stress was generated on the top surface by the motion of fine-thread (80 threads per inch) screw. Due to the different geometric sizes of poly-crystalline and single-crystalline sample, two 4-pt bending stages were designed ((a) for poly-crystalline sample, (c) for single-crystalline sample). The strain gauge is glued on top surface of the sample to measure strain. FEM model is shown in Figure 1(b). The FEM simulation is carried out using 2D plane strain element in ABAQUS 6.13. The sample elasto-plastic property in FEM model is based on an uniaxial tensile test on the sample. The tensile stress on sample top surface at certain measured strain in the experiment is then revealed through the stress in the simulation at the same strain. For single crystalline samples, when the measured strain at the top surface is larger than 0.1%, surface steps start to form (see figure 1(d)), these surface steps strongly influence indentation results at small depth, therefore, for single crystalline sample, the applied strain is up to 0.1% (to avoid forming surface steps). The bending was created by using the loading base which is pushed up by a screw. When samples are bending, the top surface is under tension. Total strain values on the top surface were recorded using uniaxial strain gauge with a resistance value of 320 Ω (National Instruments Inc., TX). The corresponding in-plane stresses were calculated by finite element (ABAQUS) simulations according to the strain values measured by the strain gauge and sample deflection. The inputs of material elasto-plastic properties in the simulations are based on the experimental data of a tensile test on the samples, assuming isotropic

elasticity. The assumption of isotropic elasticity is non-ideal but nevertheless serves as a proper starting point that should be assessed in future works. For polycrystalline samples, the measured total strain values and their stress correspondence per screw rotation are listed in Table 1. For single crystalline samples, we only strained the samples up to 0.1%, as clear surface steps were forming after 0.1% strain, these surface steps will dramatically influence and dominate the indentation results at small depth, details can be found in the supplementary material.

S2. Sample Preparation

The polycrystalline samples were prepared by the following sample preparation protocol. First, all samples were sliced by electric discharge wire machining (EDM) to a thickness of 3mm. After EDM machining, the samples were electro-polished using standard protocols [1,2] at the third party materials supplier (Materials Resources LLC, Dayton OH). The overall polycrystalline sample dimensions were 30mmx75mmx3mm. Single crystalline samples were maintained at their original dimensions (10mmx10mmx1mm from MTI Corporation., US). To measure the bulk elasto-plastic properties, standard dog bone-shaped (3.1 mm thick and 12.7 mm wide) samples were prepared and tested by 50 kN tensile tester. (MTS Insight, Eden Praire MN)

S3. Statistical Nanoindentation

Frame stiffness measurements of the 4-point loading fixture were carried out using a sapphire sample and measured as $1.516 \times 10^6 \ N/m$. It should be noted that the measured frame stiffness values were nearly constant at different stress values. It is worth noting that the frame stiffness was measured on the 4pt-bending fixture, and the same frame and Berkovich tip with corrected diamond area function was used during all indentations and stress levels. Additionally, all indentation tests were carried out in the central region of the samples where local strain is constant according to the FE simulations. For all nanoindentation experiments, the following experimental procedure was adopted. First, an aluminum test sample was placed in the 4-point loading fixture, and in-plane stress conditions were created using the motion of a set-screw with each screw rotation corresponding to 70μm deflection and verified with measured strain values. All nanoindentation tests were performed in the same 4-pt bending fixture thus the stiffness of the stage remains constant. The samples were allowed to thermally equilibrate for an hour before running indentation cycles. For poly-crystalline samples, the maximum indentation depth levels were set at 50 nm, and tests were performed with a constant loading rate of dP/dt=0.5mN/s. A total number of 5,000 indents (two 50x50 square grids) were implemented at each of nine stress levels, so the total number of indentations were ~45,000. For single-crystalline samples, the maximum indentation depth reached 150 nm with the same constant loading rate and 1,000 indents were performed at each of 4 stress levels, making the total number of indentations ~ 4,000. For the same stress level, each indent is spaced by 5 microns in each direction. After finishing indents for one stress level, the next and each successive array is offset by 100 micrometers. Using our

experimental framework, one can notice that statistically our data sets were collected using the same experimental parameters except the in-plane stress, therefore, the difference between experimental results of data sets is the consequence of the in-plane stress. During the data processing step, the obvious outliers were cleaned in a statistical manner. For detecting displacement bursts, the dynamic force oscillation was disabled during indentations. However, this option was enabled for hardness measurements, and the Oliver-Pharr continuous stiffness methodology (CSM) was used with a constant indentation strain-rate value of $0.2s^{-1}$ [3–4]. The frequency of the CSM method was set at 100 Hz. Displacements were measured with a differential capacitive sensor which has the resolution of 0.01 nm, while the environmental noise contributed a systematic error during the measurement of ~1 *nm*. The typical drift rate values were maintained at less than 0.2 nm/s.

For collecting thousands of indentation points, one of the biggest challenges is experimentation time. In general, the required time to perform only one indentation is approximately 5-7 minutes resulting in a required instrument time of 3,000 hours for each dataset (for one in-plane stress). This approach is impractical and inefficient for collecting large data sets for statistical analysis. To overcome this limitation, we implemented a new nanoindentation algorithm based on elimination of the unloading portion of the load-displacement hysteresis and scaling the indenter approach rate while keeping the initial contact rate the same as the standard indentation protocol. For the fast-protocol the total indentation time was measured to be 10s.

S4. Surface characterization of the single crystalline samples

Figure S2(a) shows the AFM measurement of our single-crystalline Al sample. The roughness fluctuates within the range of 1~ 5nm. Similar results were found for Cu samples (not shown). Figure S2(b) shows a small set of 3 indentation arrays for consecutive stress levels (0.005, 0.05, 0.1). Figure S2(c) shows force-depth curves of a large collection of indentation-samples (each sample corresponds to a different indentation location) (the inset shows force depth curves at small depths in order to compare the behavior with the similar, analogous behavior in the polycrystalline sample in Fig.1a). It can be observed that deviations exist both at small and large indentation depth. Figure 3(d) shows the average force depth curves for various strain levels. It is seen that applied stress (applied strain) leads to the decrease of the indentation force at the same indentation depth.
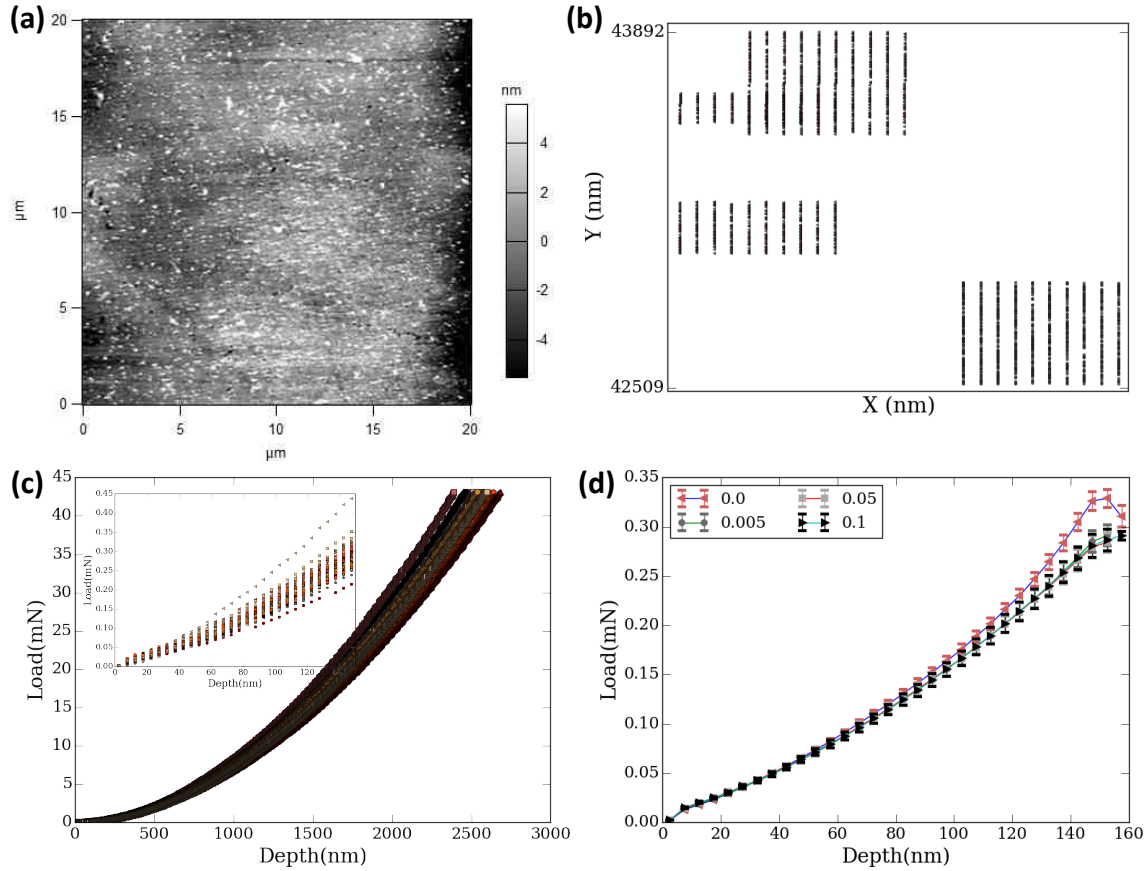
Figure S2: (a) AFM of single crystal Al, the roughness fluctuations are in the range of 1-5nm. (b) An example of a set of arrays at different stress levels: each indent is displaced by 5 microns in each direction, and for each stress level the array is displaced vertically by 100 micrometers. The arrays for 3 consecutive stress levels are shown. (c) Force-depth for a large collection of samples, showing deviations both at small and large depths. (d) Average Force-depth curves for various strain levels.

S5. Discrete Dislocation Dynamics simulation

The simulation model [5] is shown in Figure. S3: Bulk sample with length 1000 μ m and thickness 50 μ m is indented by a circular indenter with radius R=1 μ m. Applied in-plane stress was assigned prior to indentation. The finite element mesh is highly refined in the indentation region, using element size to be 0.5nm.
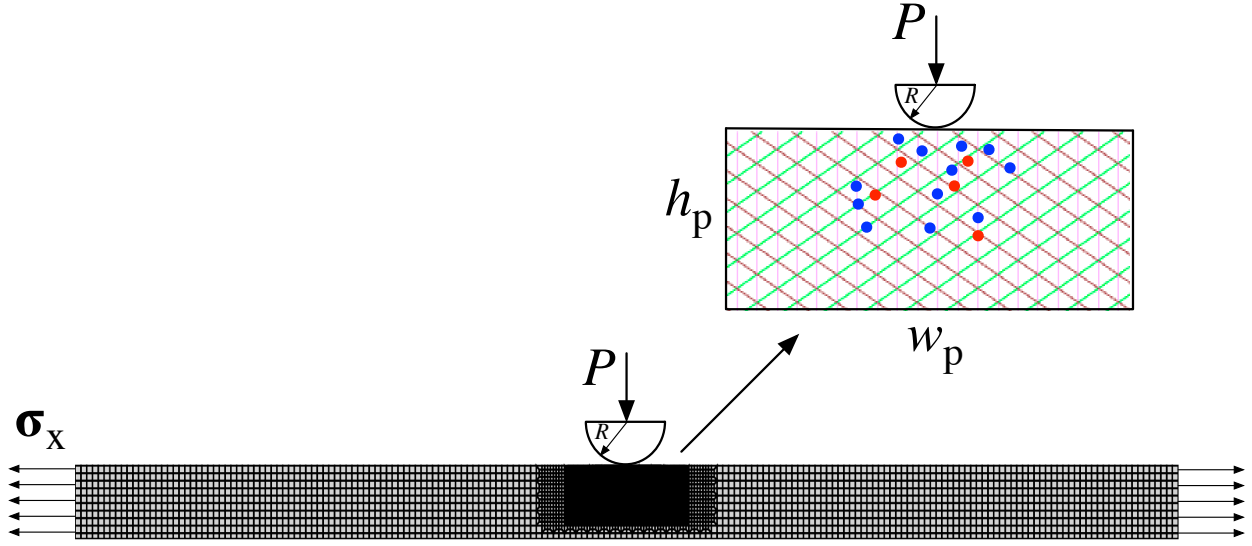
4

Figure S3: Schematic of DDD simulations. Dislocation activities are constrained in a window with size $w_p =$ 20μm, $h_p = $ 10μm. Dislocation sources (indicated by red dot) and obstacles (indicated by blue dot) are randomly distributed on slip planes.

Discrete dislocation plasticity is investigated, where small strain approximations are considered. As each dislocation is treated as a singularity, whose analytical solution is known in infinite space, this infinite space field needs to be corrected by a smooth image field (^) to ensure that actual boundary conditions are satisfied. Hence, the displacements u_i, strains ε_{ij}, and stresses σ_{ij} are written as

$$u_i = \tilde{u}_i + \hat{u}_i, \quad \varepsilon_{ij} = \tilde{\varepsilon}_{ij} + \hat{\varepsilon}_{ij}, \quad \sigma_{ij} = \tilde{\sigma}_{ij} + \hat{\sigma}_{ij},$$

where the (˜) field is the sum of the fields of all N dislocations in their current positions, i.e.

$$\tilde{u}_i = \sum_{J=1}^{N} \tilde{u}_i^{(J)}, \quad \tilde{\varepsilon}_{ij} = \sum_{J=1}^{N} \tilde{\varepsilon}_{ij}^{(J)}, \quad \tilde{\sigma}_{ij} = \sum_{J=1}^{N} \tilde{\sigma}_{ij}^{(J)}.$$

The image fields are obtained by solving a linear elastic boundary value problem using finite elements with the boundary conditions changing as the dislocation structure and the loading status evolve.

In this two-dimensional model, the FCC crystal structure is represented by three slip systems whose slip planes are oriented at $\pm 30^{\circ}$ and 90° relative to horizontal direction. Slip planes are equally spaced at d = 10b with the typical Burgers vector of FCC crystals being b = 0.25nm. We only consider glide of dislocations. The evolution of the dislocation is determined by the component of the Peach-Koehler force in the slip direction. For the I−th dislocation, this is given by

$$f^{(I)} = n^{(I)} \cdot \left(\hat{\sigma} + \sum_{J \neq I} \tilde{\sigma}^{(J)} \right) \cdot b^{(I)},$$

where $n^{(I)}$ is the slip plane normal and $b^{(I)}$ is the Burgers vector of dislocation I. This force will cause the dislocation I to glide with velocity

$$v^{(I)} = \frac{f^{(I)}}{B},$$

where B is the drag coefficient. In this paper, its value is taken as $B = 10^{-4}$ Pa s, which is representative for aluminum.

New dislocation pairs are generated by simulating the Frank-Read mechanism. In two dimensions, point sources will generate a dislocation dipole when the magnitude of the Peach-Koehler force at the source site exceeds a critical value $\tau_{nuc}b$ for a period of time t_{nuc} [1]. The initial distance between the two dislocations in the dipole is

$$L_{nuc} = \frac{E}{4\pi(1-v^2)} \frac{b}{\tau_{nuc}},$$

at which the shear stress of one dislocation acting on the other is balanced by the local shear stress.

Annihilation of two dislocations with opposite Burgers vector happens when they are within an annihilation distance of 6b.

Obstacles are included to account for the effect of blocked slip caused by precipitates and forest dislocations on out-of-plane slip systems that are not explicitly described. Dislocations get pinned when they arrive at the obstacle site. Pinned dislocations are released from the obstacles when their Peach-Koehler force exceeds an obstacle-dependent value $\tau_{obs}b$. No obstacles are permitted within $L_{nuc} = \mu b / (2\pi(1-v))\tau$ s.

At the beginning of every time increment of the simulation, nucleation, annihilation, pinning and release at obstacle sites are evaluated, and the dislocation structure is updated.

The crystal is taken to have properties that are reminiscent of aluminum with Young's modulus E = 70 GPa and Poisson's ratio $v = 0.33$.

6

Bulk sources and obstacles are randomly distributed over the slip planes with densities 300 μ m^{-2} and 2400 μm^{-2} respectively. The strength of the sources to generate edge dislocations is selected randomly from a Gaussian distribution with mean value τ_{nuc} = 50 MPa, and 10% standard deviation. The strength of the obstacles τ_{obs} is taken to be 150 MPa and 20% standard deviation. The choice of dislocation sources and obstacles properties give reasonable dislocation densities in previous nanopillar compression study [6]. The time span needed for nucleation of a dislocation dipole, t_{nuc}, is taken to be 10 ns, which is 20 × the time increment Δt used. We consider 20 random realizations for each in-plane stress case.
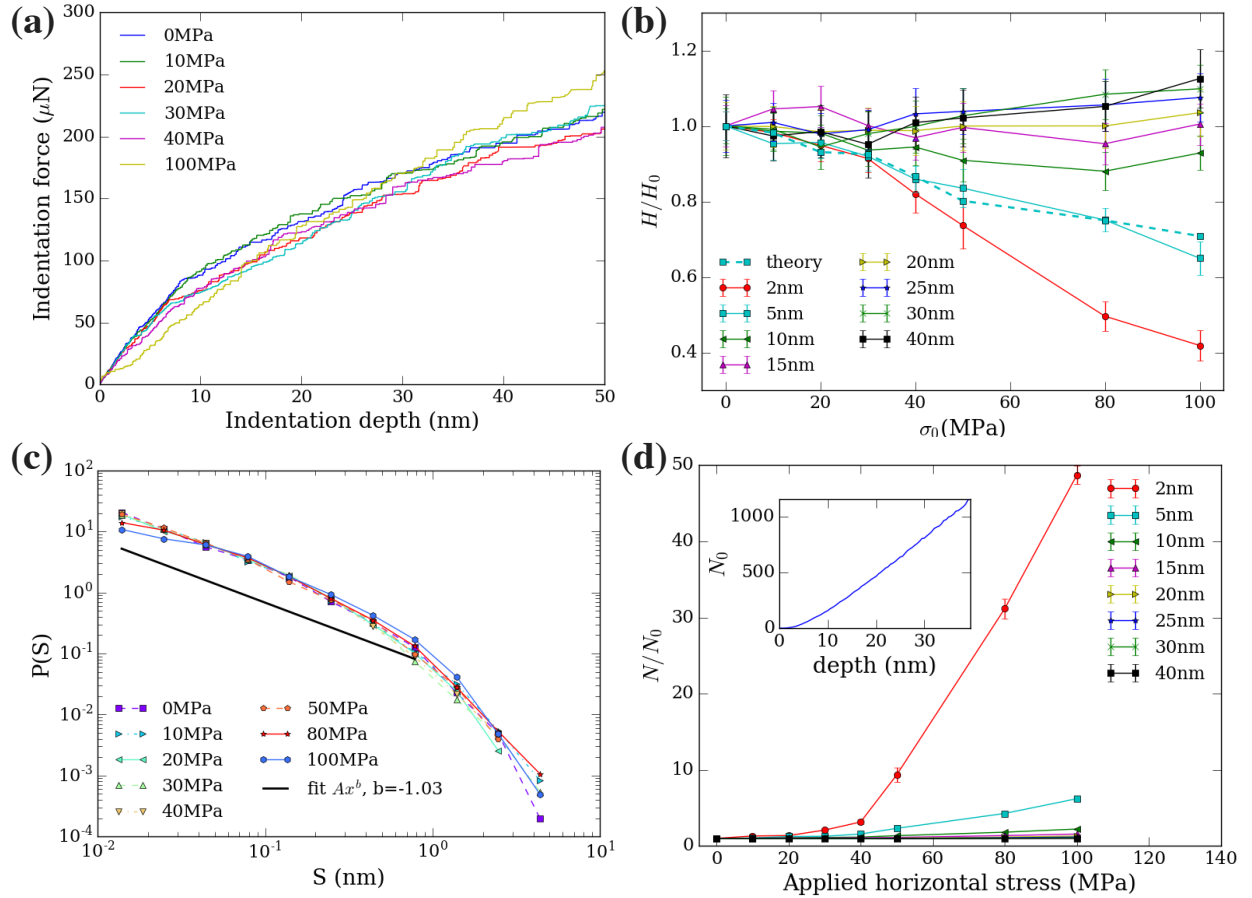

Figure 4: 2D Dislocation dynamics simulation results of bulk Al. (a) Representative load-depth curves, (b) normalized hardness deviation with respect to applied in-plane stress. The bold line is the prediction from the theoretical model for indentation depth 5nm, (c) events statistics up to 40nm indentation depth, (d) effect of in-plane stress on ta otal number of dislocations normalized by N_0 at different indentation depth. N_0 is the number of dislocations at zero in-plane stress, shown in the inset.

Figure 4b shows the normalized hardness, defined as H/H_0, where H_0 is the zero-in-plane-stress hardness measured for a specific depth. It is worth noticing that the effect of in-plane stress

on hardness varies with depth: At small indentation depths, hardness decreases with increasing in-plane stress, and this trend disappears for indentation depths larger than 5 *nm*. We identify the reason for this behavior in the dislocation density (number) evolution, shown in Figure 3d: when indentation depth is small (<10 *nm*) dislocation nucleation is scarce, and the dislocation density depends on the in-plane stress.

S6. Supplementary References

[1]   A. Barnoush, H. Vehoff, Scr. Mater. 58 (2008) 747.

[2]   D. Ma, S. Li, C. Liang, Corros. Sci. 51 (2009) 713.

[3]   G.M. Pharr, Mater. Sci. Eng. A 253 (1998) 151.

[4]   W.C. Oliver, G.M. Pharr, J. Mater. Res. 19 (2011) 3.

[5]   H. Song, H. Yavas, E. Van der Giessen, and S. Papanikolaou, S.,   Journal of the Mechanics and Physics of Solids, *123*, (2018) 332

[6]   S. Papanikolaou, H, Song, E. Van der Giessen, J. Mech. Phys. Solids 102 (2017) 17.